RSC Advances




ROYAL SOCIETY OF CHEMISTRY

www.rsc.org/advances

# Enhanced Photocatalytic Efficiency of AuPd Nanoalloy Decorated ZnO-Reduced Graphene Oxide Nanocomposites

*Bharati Panigrahy*[*a] *and D. D. Sarma*[a,b]

[a]Solid State and Structural Chemistry Unit, Indian Institute of Science, Bangalore, 560012, India

[b]Council of Scientific and Industrial Research-Network of Institutes for Solar Energy (CSIR-NISE), New Delhi, India

Inhibition of electron-hole pair recombination is the most desirable solution for stimulating photocatalytic activity in semiconductor nanostructures. To implement this, herein we study the photocatalytic efficiency of elemental Au, Pd and bimetallic AuPd nanoalloy decorated pristine and reduced graphene oxide (RGO) hybridized ZnO nanorods for degrading rhodamine 6G (R6G) dye. Fabrication of Au, Pd and AuPd nanoalloy on pristine and RGO modified ZnO nanorods is simple and more importantly surfactant or polymer free. AuPd nanoalloyed ZnO-RGO nanocomposites exhibit higher photocatalytic activity for degrading dye than both Au and Pd hybridized ones, indicating the promising potential of bimetallic nanoalloys over elemental components. A non-monotonic dependence on the composite composition was found by analyzing photodegradation efficiency of a series of ZnO-RGO-AuPd hybrid nanostructures with different weight percentages of RGO. The hybrid nanostructure ZnO-RGO(5 wt%)-AuPd (1 wt%) exhibit highest photodegradation efficiency (~100% degradation in 20 min) with an improvement in rate constant ($k$) by a factor of 10 compared to that of ZnO-RGO nanocomposite. The enhancement of the photocatalytic activity is attributed to the better separation of photogenerated charge carriers in photocatalysts thereby suggesting possible usefulness in a broad range of applications, such as sensing, photocatalysis and solar energy conversion.

**Keywords:** AuPd, Nanoalloy, ZnO, Nanorods, RGO, Photodegradation

## Introduction

Large volume of waste water produced by the textile industry is toxic and non-biodegradable.[1] Because of these aqueous wastes, the environmental pollution problems have been increasing seriously. Consequently, a great deal of investigation has been focused on the detection and treatment of pollutants often using wide band gap semiconductors.[2,3,4] Among many others in the list, ZnO nanorods have drawn increased interest in recent years due to the large band gap ~3.37 eV, high electron mobility ~200 $cm^{-2}$ $V^{-1}$ $s^{-1}$, high excitonic binding energy ~60 meV and the ability to tune the band gap over a wide range.[5,6,7] Its excellent ultra-violet light absorption and emission properties have attracted a lot of attention in the development of photoconversion devices like solar cells.[4] A major hurdle in achieving highly efficient photoconversion devices is the quick recombination of photogenerated electron-hole pairs in ZnO nanosystem.[4,8,9] A number of efforts have been made to improve charge separation and transport by hybridizing ZnO with other materials such as noble metals or carbon allotropes, which act as electron scavengers.[10,11] Graphene/reduced graphene oxide (RGO), as a member of carbon family, with a unique two-dimensional layer structure of $sp^2$ hybridized carbon atoms, has become the subject of significant research efforts due to its excellent electrical, optical, and mechanical properties.[12,13,14] Triggered by these extraordinary properties, the attention towards graphene has expanded to many areas with the idea of fabricating many new devices.[10,15,16]

In recent years, different studies demonstrated that the photoconversion efficiencies and photocatalytic property can be improved by decorating metal nanoparticles (Au, Ag, Pt etc.) on ZnO and graphene sheets assembly due to their excellent electron accepting property and synergetic effects between different components.[17-22] Enhanced catalytic properties have been demonstrated in ZnO-RGO-Ag assembly and graphene-ZnO-Au nanocomposites.[18,19] Deposition of Au or Ag nanoparticles onto ZnO was reported to greatly improve the photocatalytic reaction rate in organic degradation reactions.[20] Noble metal nanoparticles such as Au, Ag and Pt have been shown to increase the photoenergy conversion efficiency of semiconductors by extending light absorption range and increasing the effectiveness of charge carrier separation.[21,22] Among these hybrid nanomaterials, Au-ZnO nanocomposites with unique physical and chemical properties have been mostly used to improved sensing performances in CO[23] and ethanol[24], photocatalysis,[22] dye-sensitized solar cells,[25] and ultrasensitive detection of DNA[26] and proteins[27]. However, it is worth noting that in heterogeneous photocatalysis study the potential of bimetallic nanoalloys over the elemental one are relatively limited. Recently, continuous research effort has been directed for photodegradation of pollutants by using Cd-Ag,[28] Cu-Fe,[29] Pt-Cu,[30] Au-Pt[31] bimetallic nanoparticles coupled with semiconductors. Au-Ag,[32] Ni-Cu,[33] and Pt-Pb[34] alloys have been extensively used for nonenzymatic glucose detection. To the best of

our knowledge, there are no reports on Au-Pd nanoalloy decorated one-dimensional ZnO nanostructures for photoenergy conversion application till now. Furthermore, synthesis of metallic alloy nanoparticles requires surfactants or polymers to achieve stable colloidal bimetallic nanoalloys. Therefore, it is highly desirable to directly synthesize bimetallic nanoalloy in an aqueous phase and simultaneously in-situ load them onto the semiconductor or other functional materials for catalytic applications.

In this study, we prepared a new type of photocatalyst, i.e., ZnO-RGO-AuPd hybrid nanostructure, in which Au particles were first loaded on ZnO nanorod-RGO composites and then Pd nanoparticles were loaded on Au particles. The methodology of synthesis is through a one-pot aqueous route which is fast and simple without using any type of surfactant or polymer. Preliminary characterization of all hybrid nanostructures confirms the formation of elemental Au, Pd and bimetallic AuPd nanoalloy decorated ZnO-RGO nanocomposites. Subsequently, photocatalytic activities of ZnO-RGO-AuPd, ZnO-RGO-Au and ZnO-RGO-Pd have been carried out for degrading rhodamine 6G (R6G) dye establishing the higher photodegradation efficiency of bimetallic nanoalloyed ZnO-RGO nanocomposites than Au or Pd decorated ones. Shifting and increasing intensity of absorbance spectra along with quenched PL profile confirms higher photocatalytic activity of alloyed ZnO-RGO nanocomposites. By carrying out a systematic investigation of the relative composition of the composites, existence of an optimal concentration of RGO has been found to maximize the photocatalytic efficiency. The photodegradation efficiency of metal or nanoalloy decorated nanocomposites reduces in the absence of RGO. Based on our detailed investigation, a possible mechanism of the photocatalysis involved here is also presented.

## Experimental Section

**Synthesis:** Graphite (Aldrich, 99.99%) and zinc chloride ($ZnCl_2$, 99.99%, Aldrich) were used as precursors for RGO and ZnO nanorods, respectively. All other chemical reagents used in our experiments are purchased from Thomas Baker, S. D. Fine chemicals, and Finar chemicals limited. All chemicals were analytical grade reagents and used as reactants without further purification.

ZnO nanorods were prepared by an ambient thermal treatment of the precursors in aqueous condition as reported elsewhere.[35] In brief, the reaction medium was prepared by mixing 0.01 M of $ZnCl_2$ and hexamethylene tetramine (HMTA) with MilliQ water and heated at 85–90 $^oC$ for 2 hrs. Then, the milkier solution was centrifuged, copiously rinsed with MilliQ water and dried at room temperature. Graphite oxide (GO) was prepared from graphite powder by the reported modified Hummers method,[36] which has been described in our previous work.[37] For RGO synthesis, 35 mg of graphite oxide powder was dispersed in 80 mL of ethylene glycol (EG) and ultrasonicated for 1 hr to form a stable graphene oxide colloid. Subsequently, 0.8 mL of hydrazine hydrate (85 wt%) and 3.6 mL of EG solution of

NaOH (0.375 M) were added into the mixed solution. After ultrasonication for 10 min, the above mixture was transferred into a 250 mL round-bottomed flask and refluxed at 110 °C for 3 hrs under $N_2$ atmosphere. The as-synthesized solid products were separated by centrifugation, washed thoroughly with water and absolute ethanol to remove any impurities, and then dried in a vacuum oven at 50 °C for 24 h. A certain amount of as-prepared RGO (2, 5, 8, and 10 wt%) and ZnO nanorods were dispersed in water and sonicated for 1 hr to produce uniform dispersions of ZnO-RGO nanocomposites for further studies. The sample code used throughout the work for 2, 5, 8, 10 wt% RGO-ZnO nanocomposites are ZR2, ZR5, ZR8, Z10, respectively.

In the preparation of ZnO-RGO-AuPd nanocomposites, 20 mg of prepared ZnO-RGO was dispersed in 10.0 mL milliQ water and was ultra-sonicated for 1 hr. Gold(III) chloride ($HAuCl_4 \cdot 3H_2O$, 0.5 wt%) solution was added to above ZnO-RGO solution and stirring was done for 10 min. A freshly prepared $NaBH_4$ {0.01 M, $NaBH_4$/Au (mol/mol) = 5} was then added to it and solution was further stirred for 10 min. After that, equal weight (0.5 wt%) of palladium(II) chloride was added, followed by desired amount of $NaBH_4$ {$NaBH_4$/Pd (mol/mol) = 5}, to produce a dark brown solution. In order to get good interaction between ZnO-RGO and AuPd, the above reaction mixture was heated at 80 $^oC$ for 1 hr. The resultant ZnO-RGO-AuPd was centrifuged at 4000 rpm and dried at 50 $^oC$. For the synthesis of ZnO-RGO-Au (1 wt% of Au) and ZnO-RGO-Pd (1 wt% of Pd), the above reaction has been repeated without using Pd and Au precursors, respectively.

**Characterizations:** The identification and purity of the phase was tested by powder X-ray diffraction (XRD) studies using a Philips powder diffractometer PW3040/60 with Cu Kα radiation ($\lambda$ = 1.54 Å). The morphologies of the samples were examined by FEI Sirion XL30 field emission scanning electron microscope (FESEM). Transmission electron microscopic (TEM), high resolution TEM (HRTEM) images and selected area diffraction pattern (SAED) were obtained with a JEM 2100F, JEOL transmission electron microscope at an accelerating voltage of 200 kV. Raman scattering measurements were performed on Lab RAM HR800 Micro laser Raman system with a backscattering geometry using the 514 nm line of $Ar^+$ laser as an excitation source. Absorbance at the particular wavelength was recorded with a Perkin-Elmer Lambda 35 UV-visible spectrophotometer. Photoluminescence (PL) spectra were taken at room temperature following excitation with a He-Cd laser (λ=355 nm) as the light source.

**Photocatalytic Experiments:** Typically, 20 mg of photocatalysts were added to 100 mL aqueous solution of the R6G dye (20 mg/L). Before irradiation, the mixed photocatalyst and dye suspensions were magnetically stirred in the dark for 0.5 hr. Afterwards, the photoreaction vessel was exposed to the UV

irradiation (125 W) under ambient conditions. The UV irradiated suspension was analyzed at different time intervals by analyzing the variation in the intensity of maximum absorption peak of R6G dye.

**Results and Discussion**

The powder X-ray diffraction patterns of pristine ZnO, ZR5, ZR5-Au, ZR5-Pd and ZR5-AuPd hybrid nanostructures are shown in Figure 1a. The diffraction peaks of ZnO nanorods are in good agreement with the hexagonal wurtzite crystal structure ($P6_3mc$, JCPDS No. 01-080-0075) of ZnO with no impurity phase present.[35] The diffraction peaks at $2\theta = 31.7^o$, $34.4^o$, $36.2^o$, $47.5^o$, $56.5^o$, $62.8^o$, $66.3^o$, $67.9^o$ and $69.0^o$ corresponding to the characteristic ZnO crystal planes of (100), (002), (101), (102), (110), (103), (200), (112), and (201), respectively. The XRD peak positions of the hybrid nanostructures are identical to those of ZnO; however, presence of a broad and weak diffraction peak at around $2\theta = 24.5^o$ (Inset of Figure 1a) for all the hybrid nanostructures corresponds to the (002) diffraction peak of graphene (JCPDS No. 01-0646) with an interlayer distance (*d*-spacing) of 0.36 nm, which is slightly more than the *d*-spacing of perfect graphene.[38,39] Thus, the XRD patterns confirm these samples to be hybrid nanostructures, comprised of ZnO wurtzite crystals and few layer graphene sheets where the diffraction peak related to metal may be lost in the background noise due to its low concentration (1 wt%) in the nanocomposite. To confirm the formation of AuPd nanoalloy, we have carried out the XRD scan on Au, Pd and AuPd nanoparticles presented in Figure 1b. The XRD peaks of as synthesized nanoparticles can be indexed as the face-centre-cubic (fcc) structure of Au and Pd. In addition, it can clearly be observed that the XRD peaks of AuPd nanoalloy situated in between those of pure Au and Pd nanoparticles. According to Vegard's law, the diffraction peak of the metal alloy should lie between the two set peaks of the pure metals. Therefore, diffraction angle position proves that the AuPd nanoparticles demonstrate an alloy pattern.[39,40]

Raman spectra of the as-prepared ZnO, ZR5, ZR5-Au, ZR5-Pd and ZR5-AuPd hybrid nanostructures (Figure 2) show typical features of carbon materials: the G band (1589 $cm^{-1}$) is assigned to the in-plane stretching motion of symmetric $sp^2$ C−C bonds, whereas the D band (1350 $cm^{-1}$) results from the disruption of the symmetrical hexagonal graphitic lattice.[41] In general, intensity ratio of the D band ($I_D$) to the G band ($I_G$) is a measure of the degree of disorder and the average size of the $sp^2$ domains in graphitic materials. However, this intensity ratio ($I_D/I_G$=1.14, 1.16, 1.19 and 1.21 for ZR5, ZR5-Au, ZR5-Pd, and ZR5-AuPd, respectively) of the hybrid nanostructures is much higher than that of GO (0.99, Figure S1), which indicates a decrease in the average size of the in-plane $sp^2$ domains upon reduction of GO.[42,43] Inset of Figure 2 shows the Raman spectrum of ZnO nanorods. The most intense peak at 437 $cm^{-1}$ corresponds to the non-polar optical phonon mode of ZnO (high frequency $E_2$ mode)

in hexagonal wurtzite structure. In addition to this first-order Raman mode, the spectrum also shows a band at 332 $cm^{-1}$, corresponding to the second-order phonon mode of ZnO (low frequency $E_2$ mode). In ZnO-RGO nanocomposite spectrum, the predominant high frequency $E_2$ mode peak of ZnO located at ~434 $cm^{-1}$ indicates the wurtzite structure is preserved. This shift of ~3 $cm^{-1}$ of the higher frequency phonon mode has been attributed to the interaction of ZnO and RGO sheets.[44] Similarly, the shift of 4, 3, and 3 $cm^{-1}$ for ZR5-Au, ZR5-Pd, and ZR5-AuPd, respectively, is due to the interaction between metal nanoparticles and nanoalloy with ZR5 nanocomposite. The XRD pattern and Raman spectra clearly confirm the formation of wurtzite-type ZnO crystal structure in all the hybrid nanostructure by us.

Figure 3 shows morphologies of ZnO-RGO nanocomposites and metal hybrid nanostructures. The FESEM image of ZnO-RGO nanocomposite (Figure 3a) confirms the formation of ZnO nanorods embedded in RGO sheets, with an average diameter of 120 nm and length of around 4-5 μm. ZnO nanorods are well spread out on the RGO sheets. The contrast provided by these RGO sheets is very low, because of the thinness of the sheets. Figures 3b show the TEM images of 5 wt% RGO-ZnO nanocomposites consisting of two-dimensional RGO encapsulated with ZnO nanorods. From the TEM image of RGO (Inset of Figure 3b and Figure S2), thin sheets larger than several micrometers with wrinkles are observed. The SAED pattern (Inset of Figure 3b) confirms that the nanorods are single crystals belonging to hexagonal ZnO and are grown along the *c*-axis [0002] direction. Figure 3b indicates a partial disappearance of wrinkles of RGO sheets caused by the encapsulation of ZnO nanorods. Decoration of AuPd nanoalloy on the surface of RGO covered ZnO nanorod is observed in Figure 3c. The sizes of AuPd nanoalloy are varied from 5 to 10 nm as indicated in the TEM image (Figure S3). Uniform contrast throughout the TEM image confers the formation of AuPd bimetallic nanoalloy instead of mixed Au and Pd nanoparticles (Figure S3). Energy-dispersive X-ray spectroscopy on 10 different locations confirms 1:1 ratio of AuPd nanoalloy in the sample. Attachment of Au and Pd nanoparticles on the ZnO-RGO nanocomposites is confirmed by TEM analysis (Figure S4). Calculated lattice spacing from the HRTEM image (Insets of Figure S4) illustrate (111) planes of face-centered cubic Au (0.236 nm) and Pd (0. 225 nm) nanoparticles.[39] Figure 3d demonstrates the HRTEM image of ZR5-AuPd hybrid nanostructure, where the calculated lattice spacing of ZnO (0002) and AuPd (111) nanoalloy is 0.52 nm and 0.23 nm (Figure S3), respectively.[39] Reduction potential of $Pd^{2+}$/Pd (standard reduction potential $E^0$ = +0.951 V) and $AuCl_4^-$/Au ($E^0$ = +1.000 V) are almost in the same level.[45,46] So the formation of AuPd nanoalloy particles by the presented method is feasible. There is an intimate contact between ZnO nanorods, RGO sheets, metal nanoparticles and nanoalloy suggested by both the suppression of wrinkles of RGO sheets, and the shift of the high frequency Raman signal of ZnO (Figure 2), indicating substantial interaction between all the components of the composite material. This

helps in a facile separation of photo-generated charge carriers in ZnO, which may be responsible for the remarkable enhancement of optical properties and photocatalytic performance presented below.

The absorption spectra of pristine and RGO-modified ZnO nanocomposites (2-10 wt%) are presented in Figure 4a. The inset shows that pure RGO has an absorption maximum at 263 nm, while that for ZnO nanorods is at 369 nm. The absorption band at 263 nm for RGO is due to the excitation of the π-π* transition in the graphitic structure (C=C).[47,48] The UV–visible absorption spectra of bulk ZnO has been reported to appear at 378 nm,[49] defining a distinct blue shift of the absorption edge of ZnO nanorods by ~9 nm from 378 to 369 nm due to their shape and size.[50] The absorption spectra of the composite samples, shown in the main frame of Figure 4a, clearly show distinct features arising from RGO at about ~263 nm and ZnO nanorods at about 369 nm. The spectral shape is consistent with the composite nature of the sample. Figure 4b shows the absorption spectra of Au, Pd and AuPd nanoalloy decorated ZR5 nanocomposite. The absorption maximum in the case of ZnO at 369 nm is red shifted to 373, 375, and 379 nm for ZR5-Au, ZR5-Pd and ZR5-AuPd, respectively. The observed red shift in the absorption band position is due to the discharge of photogenerated electrons accumulated on the conduction band of ZnO nanorod.[18] Shift is large for ZR5-AuPd nanocomposites compare to that of ZR5-Au and ZR5-Pd, as AuPd nanoalloy withdraws electron density more towards itself, which affect the movement of the band position of ZnO. In addition, a significant increase in absorbance intensity of nanoalloy decorated nanocomposites in the UV (till 420 nm) region has also been observed, indicating the absorbance range increases for hybrid nanostructures. Therefore, increase in the light harvesting efficiency and the absorbance range of metal and nanoalloy decorated ZnO-RGO nanocomposites clearly demonstrates that these materials become more photoactive.

Room temperature PL spectra from pristine and various wt% of RGO modified ZnO nanorods, metal nanoparticles and nanoalloy hybridized nanocomposites were recorded to probe possible interactions between metal or nanoalloy, RGO and ZnO in the hybrid nanomaterial (Figure 5). PL spectra of all samples, including pure ZnO nanorods, show a weak and sharp emission peak centered at around 390 nm and a more intense, broad emission band ranging from 450 to 800 nm. This is typical of most emission spectra from nano-sized ZnO systems, with the sharp emission in the UV region arising from the radiative recombination of electron-hole pairs across the band gap, the near-band-edge (NBE) or the excitonic emission. The broad band emission at longer wavelengths arises from defect or surface states of ZnO. [50-52] It is important for our purpose to note here that the absorption in pure ZnO nanorods in our case generating electron-hole pairs across the band-gap decays dominantly via the surface states, making the integrated emission intensity in the longer wavelength component much larger (~5 times) than that of the excitonic emission at 390 nm.

In order to follow the effect of RGO on the relative intensities of these two emission features, we have shown the emission spectra from composites with a varying RGO content by normalizing the spectra at the excitonic emission in Figure 5a. This figure makes it clear that there is a strong preferential quenching of the emission arising from the surface states with an increasing RGO content. When ZnO-RGO nanocomposite is modified with metal nanoparticles and AuPd nanoalloy, the intensity of PL emission is seen to be drastically quenched. Figure 5b shows the emission spectra of ZR5, ZR5-Au, ZR5-Pd and ZR5-AuPd normalized at the excitonic emission. The significant decrease in the surface emission feature, ranges from 450-800 nm, suggests a substantial coupling of the surface states of ZnO nanorods with RGO, Au, Pd and AuPd derived states in the composites. In order to understand the impact of RGO coupling to ZnO nanorods, and the effect of metal and nanoalloy on the excitonic and surface state emissions separately, we have plotted the emission spectra of all samples normalized by the absorbance of the sample at 369 nm, representing the ZnO contribution in Figure 5c and 5d, respectively. Figure 5c establishes that both excitonic and surface state emissions are suppressed with increasing RGO content. Figure 5d clearly shows a spectacular suppression of the surface state emission with the incorporation of metal nanoparticles and nanoalloy in ZR5 nanocomposite. The effect of RGO is easily understandable, since the coupling of ZnO nanorods with RGO will be controlled primarily by the wave-function residing largely on the outermost surface atoms of ZnO due to their spatial proximity with the RGO wave-functions. Such coupling of RGO and ZnO states will be considerably weaker for ZnO excitonic states, whose wave-functions have weight throughout the nanorods and not preferentially at its surface. Figure 5d demonstrates greater quenching of both excitonic and defect related emission for metal nanoparticles and nanoalloy decorated ZR5 nanocomposites. The relatively lower intensity bands for ZR5-AuPd indicate enhanced inhibition of electron-hole pair recombination, as compared to the elemental decorated ones. PL spectrum of ZR5-AuPd hybrid nanostructure exhibits 88% and 86% drop in excitonic emission, whereas the defect related emission is reduced by 97.5% and 93% with respect to pristine ZnO and ZR5 nanocomposite, respectively. These results illustrate that the incorporation of metal or nanoalloy in ZR5 nanocomposite inhibit direct and defect-related charge carrier recombination in a very effective manner.

We have carried out a systematic investigation on the photodegradation of R6G dye in solution with pristine and different wt% of RGO modified ZnO nanorods, Au, Pd, and AuPd decorated ZnO-RGO nanocomposites as photocatalysts. The dye concentration was measured by using UV-visible absorption spectrum of R6G, which were recorded before and after UV irradiation up to a maximum of 3 hrs. The absorption intensity of R6G solution in presence of pristine ZnO (Figure S5), indicating a moderate level of photocatalytic activity of ZnO nanorods themselves in degrading R6G. Figure 6a,

illustrating the degradation of R6G in presence of ZR5 nanocomposites, makes it evident that the photocatalytic activity of ZnO nanorods is enhanced by the encapsulation of RGO. We note here that pure RGO does not have any such photocatalytic activity as confirmed by us in a control experiment with R6G solution in presence of only RGO. This suggests that an energetically favored interface between ZnO nanorod and RGO sheets, in the hybrid structure plays an important role in the enhancement of photocatalytic activities. Shao *et. al.*[53] has reported a similar kind of photodegradation study for Rhodamine B (RhB) dye by using thorn-like ZnO-multiwalled carbon nanotube (MWCNT) hybrid. Incorporation of MWCNT hybrid paper in ZnO system demonstrates excellent photo-degradation of RhB dye within 90 minutes, with good recyclability. Here, the progression of R6G photodegradation by pristine ZnO nanorods and that for all RGO-ZnO composite photocatalysts are shown as a function of time in Figure 6b. A blank run confirmed that the concentration of R6G is hardly reduced under UV light irradiation in the absence of any of the photocatalysts, while the photocatalytic degradation efficiency is found to be ~30% after 3 hrs of irradiation for pristine ZnO nanorods. Figure 6b shows that the degradation efficiency is rapidly increased in presence of RGO to 68% for ZR2 and reaches the maximum value of 89% for ZR5 nanocomposite at the end of 3 hrs. By increasing the RGO concentration above 5 wt%, the photodegradation efficiency reduces systematically, as shown in the Figure 6b, establishing to a well-defined optimal value of RGO concentration for the photocatalytic activity.

In order to explore the effectiveness of as-synthesized Au, Pd nanoparticles and AuPd nanoalloy on ZnO-RGO nanocomposites, the photocatalytic activities of ZR5-Au, ZR5-Pd and ZR5-AuPd were monitored under UV radiation. Distinctly enhanced photocatalytic efficiency was observed with the addition of ZR5-AuPd nanocomposite as presented in Figure 6c. A rapid decomposition of the dye confirms 100% degradation can be achieved by ZR5-AuPd photocatalyst within a short time of 20 min. However, for ZR5-Au and ZR5-Pd, the concentration of R6G dye (absorbance spectra, Figure S6) is reduced by 100% in the time period of 45 and 35 min, respectively. As presented in Figure 6d, a significantly faster photocatalytic performance was observed with ZR5-AuPd nanocomposite, as compare to ZR5-Au and ZR5-Pd. Figure S7 shows the photodegradation rates of R6G using ZnO-RGO-AuPd photocatalysts with different (2-10) wt% RGO, which can be used to compare the effect of RGO concentration on the photocatalytic activities of ZnO-RGO-AuPd. It is clear that 5 wt% is the optimal wt% of RGO for the ZnO-RGO-AuPd photocatalysts as demonstrated in case of ZnO-RGO nanocomposites system (Figure 6b) without AuPd alloying. It is noteworthy that when the amount of RGO is above 5 wt%, the photocatalytic activities of as-synthesized photocatalysts decrease greatly with increasing amounts of RGO. The decrease in the photocatalytic efficiency with increasing RGO content

beyond the optimal value of 5 wt% (Figure S7 and 6b) is presumably due to the reduction in the absorption of photons by ZnO nanorods in the presence of excessive RGO, absorbing in the shorter wavelengths. We have also examined the degradation efficiency of the above mentioned hybrid nanostructures without RGO, i.e. ZnO-Au, ZnO-Pd and ZnO-AuPd presented in Figure 6d. It is clear that by using ZnO-Au, ZnO-Pd and ZnO-AuPd photocatalysts, only 30%, 38%, and 50% of the dye can be degraded in 20 min, while longer reduction time of 90, 80 and 50 min, required for degrading 100% of the dye (Figure S8), respectively. From the above analysis we can interpret the important role of RGO in the degradation process as it plays a critical role in the efficient photocatalytic reduction of R6G. We have again analyzed the role of RGO by synthesizing ZnO-Au, ZnO-Pd and ZnO-AuPd first and then mixing 5 wt% of RGO by ultrasonication for 1 hr. The concentration of dye and used amount of photocatalyst is kept same as used in previous reactions. In the photodegradation process displayed in Figure S8, it is found that ZnO-Au-RGO and ZnO-Pd-RGO have better photocatalytic activity compared to the photocatalysts prepared without RGO, i.e. ZnO-Au and ZnO-Pd. However, ZR5-Au, ZR5-Pd and ZR5-AuPd need less dye degradation time than ZnO-Au-RGO, ZnO-Pd-RGO and ZnO-AuPd-RGO, respectively. These results prove that under UV light ZR5-AuPd photocatalyst has improved performance than the other hybrid nanostructures prepared.

Plots of $\ln(C_t/C_o)$ against time, 't' (Figure S9) suggest that the photocatalytic degradation kinetics follows the pseudo-first-order rate equation,[54] with a good linear correlation with the reaction time for all catalysts. Here, $C_o$ and $C_t$ are the absorbance of R6G solution (absorption spectrum) at the initial time and after a time 't', respectively, as the absorbance of the dye during photodegradation is proportional to its concentration. The rate constant ($k$) values are obtained from the negative slopes of the straight lines from $\ln(C_t/C_o)$ *vs* 't' plot for different catalysts and are presented in Figure 7a. The rate constant value for the nanocomposites containing 5 wt% RGO is estimated to be more than five times larger than that of pristine ZnO nanorods. By incorporating Au and Pd on ZR5 nanocomposite, the rate constant values (Figure S9) are $0.37\text{x}10^{-1}$ $\text{min}^{-1}$ and $0.45\text{x}10^{-1}$ $\text{min}^{-1}$, respectively following the similar pseudo-first order kinetics. Using ZR5-AuPd photocatalyst, the dye degradation rate constant value is drastically improved to $1.12\text{x}10^{-1}$ $\text{min}^{-1}$, which is 3 and 2.5 times greater than ZR5-Au and ZR5-Pd, respectively. Compared to ZR5, there is an increment of 3.2, 4, and 10 fold in the rate constant values for ZR5-Au, ZR5-Pd and ZR5-AuPd photocatalysts, respectively. The enhancement can be assigned to the presence of elemental nanoparticles and bimetallic nanoalloy over the surface of ZnO-RGO nanocomposites, which modifies the charge separation process, resulting in great improvement of the apparent rate constant of the R6G photodegradation process. These observations illustrate that Pd

decorated ZR5 exhibits the higher rate constants compared to that of Au, while AuPd nanoalloy decorated ZR5 has the maximum rate constant.

In order to understand the mechanism of this photocatalytic degradation, we note that the excitation energy equal to or higher than the band gap of ZnO results in the excitation of an electron from the valence band to the conduction band. The photogenerated electrons and holes, if separated from each other, may give rise to the following reactions:

$ZnO + h\nu \rightarrow ZnO(e^-_{CB} + h^+_{VB})$ ----------(1)

$h^+_{VB} + dye \rightarrow$ oxidation of dye ----------(2)

$h^+_{VB} + H_2O \rightarrow H^+ + {}^*OH$ ----------(3)

${}^*OH + dye \rightarrow$ degradation of dye ----------(4)

The formation of the hole in the valance band can lead to a direct oxidation of the dye (Eq. 2 above) or to the generation of hydroxyl radicals (Eq. 3 above) that may lead to the degradation of pollutants (Eq. 4 above).[55,56] In such a photocatalytic process, recombination of photoinduced charge carriers in Eq. 1 above is a primary cause to reduce the efficiency of photocatalyst. The fabrication of ZnO-RGO nanocomposite is an effective way for improving the photocatalytic efficiency, primarily because RGO can act as an electron scavenger from photoexcited ZnO (Figure 5c), thereby making the holes in ZnO available for photocatalytic reactions, shown in Eq. 2-4 above. The photo-generated electron from the ZnO nanorods can transport along the RGO sheets and then interact with the absorbed $O_2$ to form holes and OH radicals for R6G dye degradation. Here, RGO serves as an electron collector as well as transporter to delay electron-hole recombination in ZnO system.[57] On the other hand, with ZR5-Au, ZR5-Pd and ZR5-AuPd, the presence of Au, Pd and AuPd nanoparticles effectively adsorb electrons from RGO sheets (Figure 5d) and hence prevent the immediate recombination process, increase the lifetime of the photo-excited electrons. Subsequently, charge separation in the nanocomposites can be greatly enhanced due to the hindrance of the electron-hole recombination caused by the effective charge transfer between ZnO, RGO and metal nanoparticles. This phenomenon gives rise to a large number of holes, leading to the higher photocatalytic efficiency of the mentioned photocatalysts.

We have verified that the absorption of photons by the ZnO nanorods is crucial for the photocatalytic activity in two different ways. As already mentioned, our control experiments show that RGO alone has no such activity, while pure ZnO nanorods show a moderate level of photocatalysis under UV radiation (Figure 6b). To understand the role of individual AuPd and RGO-AuPd as a

photocatalyst in ZR5-AuPd hybrid nanostructure, we carried out the photodegradation experiment separately by using the same concentration of AuPd nanoalloy and RGO-AuPd taken in ZR5-AuPd. AuPd nanoalloy and RGO-AuPd show negligible degradation efficiency (Figure S10) confirms the passive role as a photocatalyst in ZR5-AuPd hybrid nanocomposites to degrade the dye. Additionally, we verified that the photocatalytic activity is absent in the absence of any UV radiation by cutting off the UV part of the incident light with the use of a glass slide (Figure 7b). Based on the above observations, the proposed mechanism of photocatalytic activity is displayed in Scheme 1. The Fermi level of RGO (–4.42 eV), which lies below the conduction band of ZnO (–4.05 eV), energetically favours the transfer of electrons from ZnO to RGO. Its great electrical conductivity and higher carrier mobility than ZnO, lead to facile scavenging of photogenerated electrons, giving rise to the efficient photocatalytic reduction. On the other hand, the work functions of Au and Pd are –4.70 and –5.12 eV, respectively which lies below the energy level of RGO. Therefore, the electrons removed from ZnO by RGO are easily transferred to these metals. This charge separation process effectively increases the lifetime of electron in the nanocomposites. Accumulated charges with lengthier lifetimes can generate more holes in the system which will perform faster photodegradation. The well defined interface between ZnO, RGO and metal nanoparticles of nanocomposites can play an important role in the enhancement of charge transfer activities. The higher work function value of Pd as compared to Au make ZR5-Pd more-effective as an electron acceptor.[58,59] The work function of AuPd alloy lies in between –5.10 and –5.12 eV, lower than that of Au, but comparable to that of Pd.[46] However, the significantly improved catalytic property of AuPd decorated nanocomposites is possibly due to changes in the details of the electronic structure on alloying of Au and Pd. In case of AuPd nanoalloy, the energetically favourable states to accept electron from higher energy levels are more compare to Au or Pd.[60,61] This suggests that the charge transfer from RGO to bimetallic AuPd nanoalloy counterpart is more efficient than to elemental nanoparticles, leading to the rapid reduction of R6G dye within 20 min. To support the above argument, the red-shift of absorbance spectra confirms the electron trapping nature of ZR5-AuPd photocatalysts tends to better photocatalytic activity. These results are also in line with PL studies presented in Figures 5b and 5d, where the drop in excitonic and defect related emission intensities is maximum for ZR5-AuPd. The reusability of ZR5-AuPd photocatalyst have been investigated by performing 3 cycles of photodegradation experiment under UV light and the reduction rate is presented in Figure S11. The degradation results show 95.9%, 92.5% and 87.2% of dye degradation is observed within 20 min of time after first, second and third cycle, respectively. Slight decrease in the degradation rates has been observed which is mainly due to loss of the ZR5-AuPd photocatalyst through centrifugation/wash processes.

In order to assess the role of the proposed oxidation of water and the consequent generation of hydroxyl radicals in the photocatalytic process (Eq. 3 and 4 above), we carried out the same photocatalytic reactions, as shown in Figure 6b and 6d, but in presence of increased $OH^-$ by varying the pH of the solvent with the addition of NaOH.[62] As presented in Eq. 2, holes play an important role for the direct oxidation of dye in photocatalytic processes. By using hole scavenger thiocyanate ion, Udawatte *et. al.*[63] confirmed inhabitation of degradation reaction. To investigate the actual role of hydroxyl radicals in the photocatalytic activity, the pH of the solvent was varied. As we can see from Figure 7b, the photocatalytic efficiency of the ZnO nanorods increases from 30 to ~38% and ~42% with pH 8.5 and 10, respectively. A similar trend is seen for ZR5 photocatalyst at pH 10 with a moderate increase in the efficiency from 89 to 91% after completion of 3 hrs. Whereas, for ZR5-Au, ZR5-Pd and ZR5-AuPd hybrid nanostructures, the photocatalytic efficiency value increased from 43 to 45%, 48 to 52%, and 82 to 85% in 15 min, respectively (Figure 7c). This photodegradation result confirms that the photogenerated holes and hydroxyl radicals both can play a major role when catalysis experiments are performed under UV light. The examined photocatalyst is eco-friendly, efficient, and reusable for the degradation of dyes, without producing toxic by-products. Our study opens up a new class of hybrid nanostructure that can be used effectively to degrade R6G and other potential dyes used in the textile industries.

**Conclusions**

In summary, elemental nanoparticles (Au, Pd) and AuPd nanoalloy decorated RGO modified ZnO photocatalysts were synthesized by a simple aqueous route without using any surfactant or polymer. The structural and optical properties were studied by XRD, Raman, UV-visible, and PL spectroscopy. RGO layers, Au, Pd, and AuPd act as traps for the photogenerated electrons, causing the quenching of near band-edge emission as well as defect emissions of ZnO nanorods, thereby increasing the photocatalytic activity of ZnO nanorods. Incorporation of 1 wt% of Au, Pd or AuPd in ZnO-5 wt% RGO nanocomposites significantly improves the rate of photodegradation by 3.2, 4 and 10 times, respectively than that of the ZR5 composite. RGO matrix acts as an inhibitor toward the hole and electron recombination, and AuPd nanoalloy assisted in efficient charge separation that helps the excited holes and hydroxyl radicals for degradation of dye. Therefore, it can be concluded that AuPd nanoalloyed ZnO-RGO composite can be effectively used for degrading pollutants in water more efficiently with possible applications in the area of water splitting and energy conversion devices.

**Acknowledgements**

Financial support from INSPIRE Faculty Scheme of Department of Science and Technology (DST), Government of India is greatly acknowledged. The authors are grateful to Indian Institute of Science for providing all characterizing tools. The instrumental support for PL measurement from Prof. K. K. Nanda and Satish Shinde, Dept. of MRC, IISc is highly acknowledged.

**Figures with Captions**

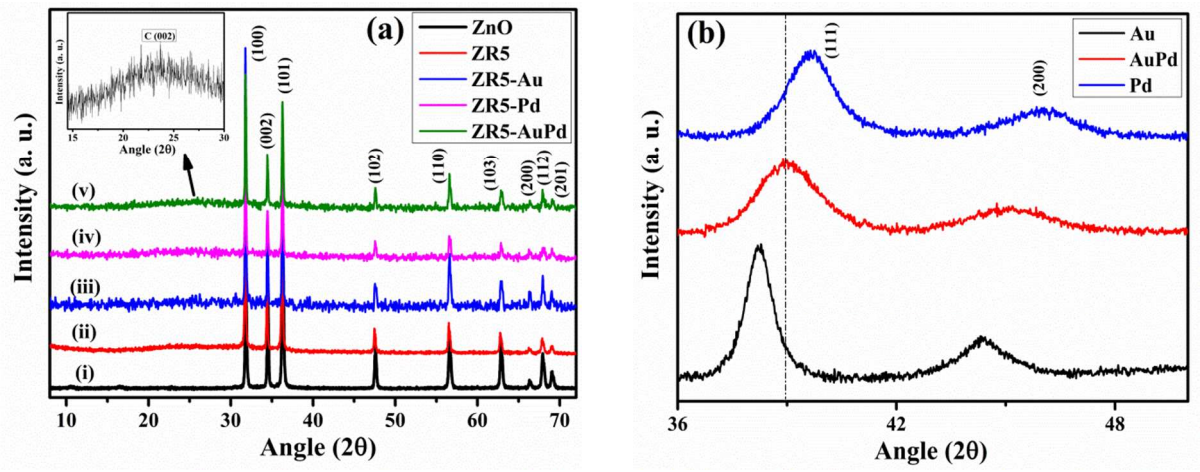


**Figure 1:** Powder XRD patterns taken from (a) ZnO and its nanocomposites: (i) pristine ZnO nanorods, (ii) ZR5, (iii) ZR5-Au, (iv) ZR5-Pd, and (v) ZR5-AuPd hybrid nanostructures, and (b) metal and metal alloy nanoparticles.

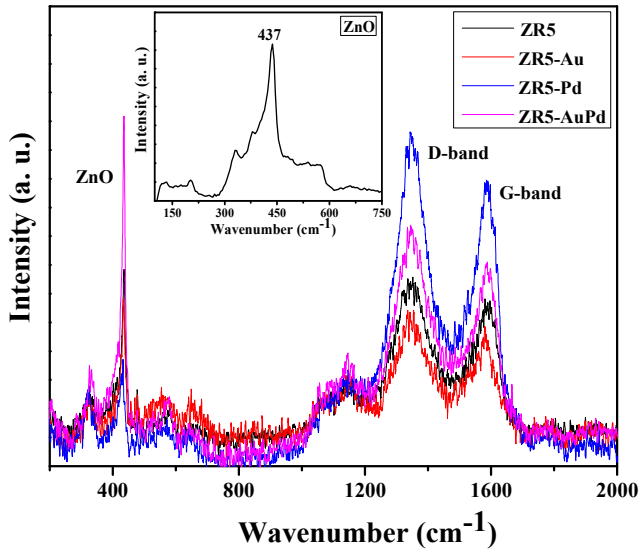


**Figure 2:** Room-temperature micro-Raman spectra of ZR5, ZR5-Au, ZR5-Pd, and ZR5-AuPd hybrid nanostructures. Inset shows Raman spectrum of pristine ZnO nanorods.

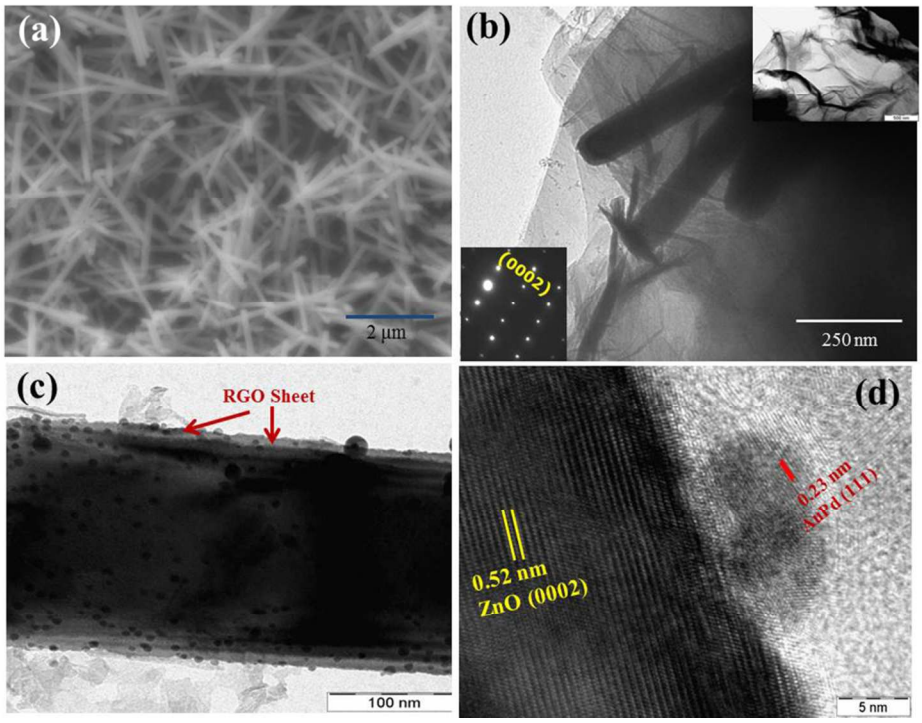


**Figure 3:** (a) FESEM and (b) TEM image of ZR5 nanocomposite. (c) TEM and (d) HRTEM images of ZR5-AuPd hybrid nanostructures. Inset of (b) shows TEM image of RGO sheet and SAED pattern of ZnO nanorods confirms the single-crystalline and [0002] directional growth.

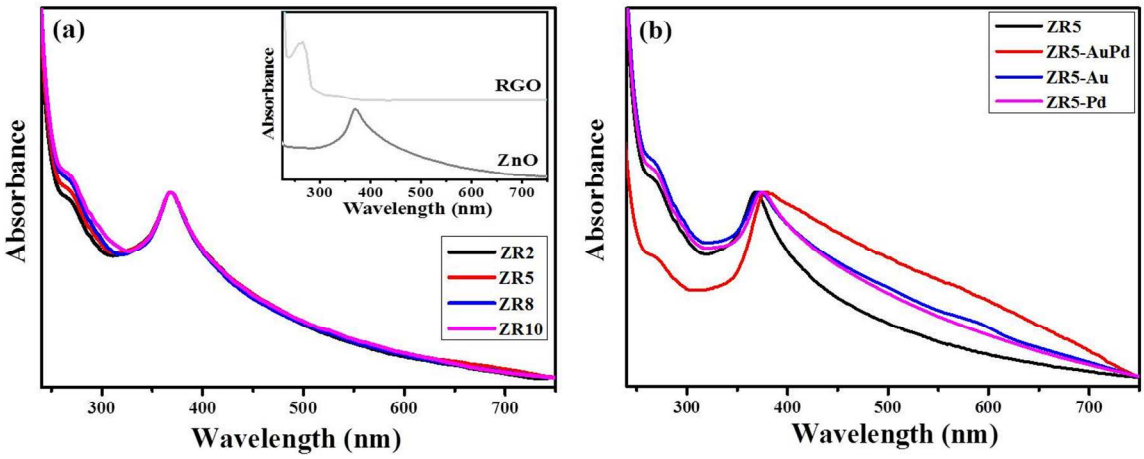


**Figure 4:** Experimental UV-visible absorption spectra of (a) RGO-ZnO composite samples with varying composition and (b) ZR5-Au, ZR5-Pd and ZR5-AuPd hybrid nanostructures, as shown in the legend. The inset of (a) shows the UV-visible absorption spectra of ZnO nanorods and RGO sheets separately.

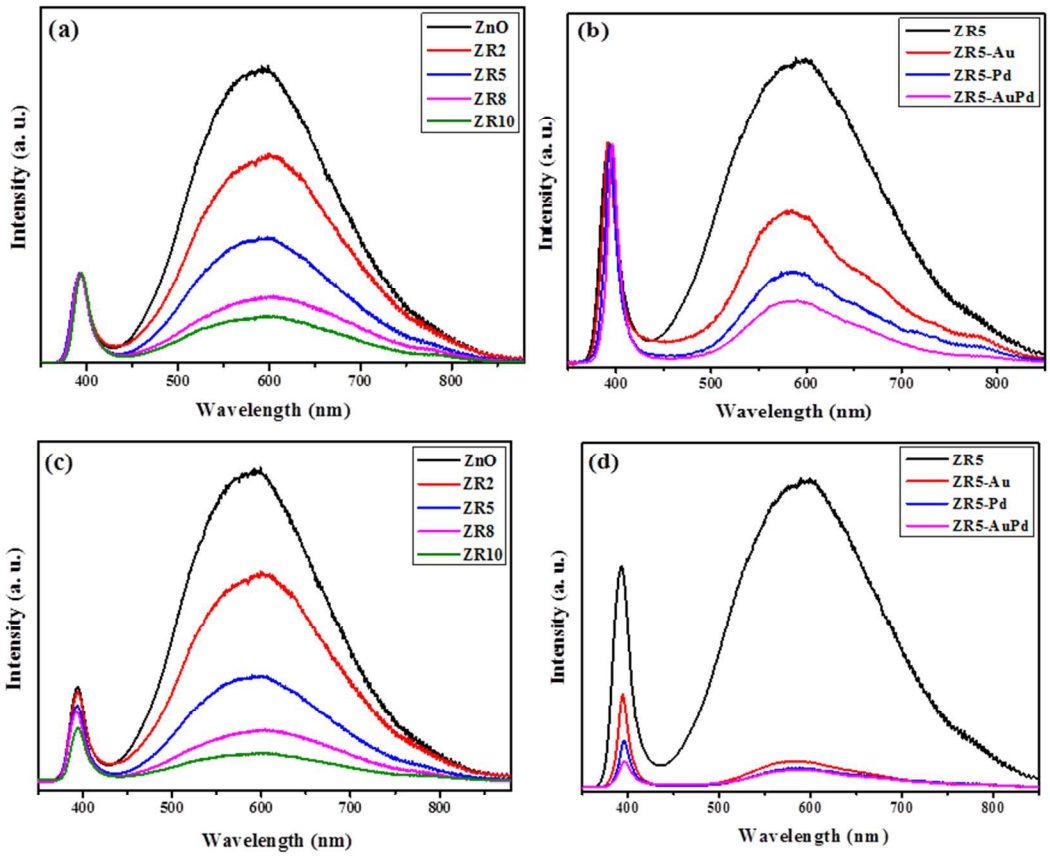


**Figure 5:** Room temperature PL spectra normalised with respect to the excitonic peak of ZnO i.e. centred at 390 nm; (a) ZnO and various wt% ZnO-RGO nanocomposites, and (b) Au, Pd and AuPd decorated ZR5 nanocomposites. PL spectra normalised with respect to the UV-visible absorbance spectra; (c) ZnO and various wt% ZnO-RGO nanocomposites and (d) Au, Pd and AuPd decorated ZR5 nanocomposites.

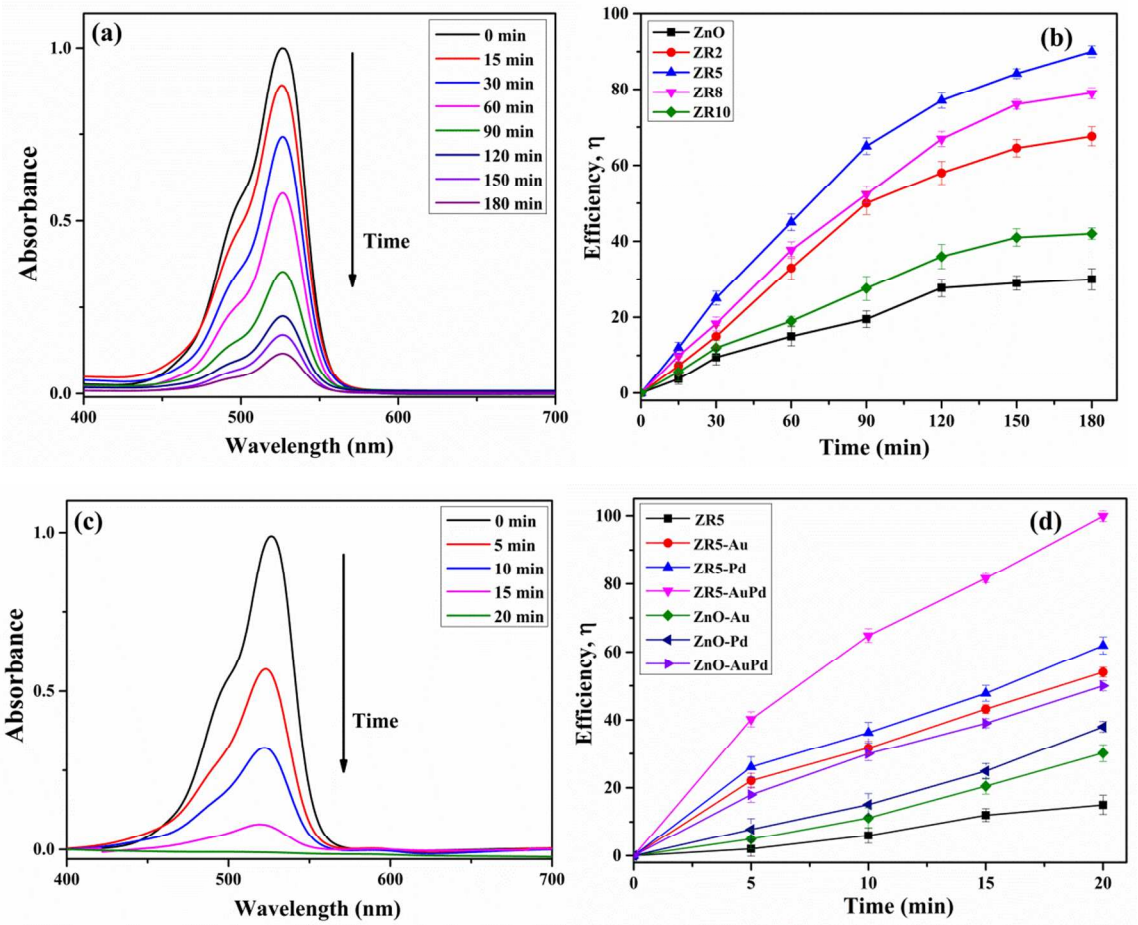


**Figure 6:** Time dependent (UV light irradiation) UV-visible absorption spectra of R6G dye degraded by (a) ZR5 and (c) ZR5-AuPd hybrid nanostructures. The efficiency of dye removal, η (with error bars), in the presence of photocatalysts (b) ZnO and various wt% of RGO modified ZnO nanorods, and (d) Au, Pd and AuPd decorated ZR5 nanocomposites as a function of irradiation time.

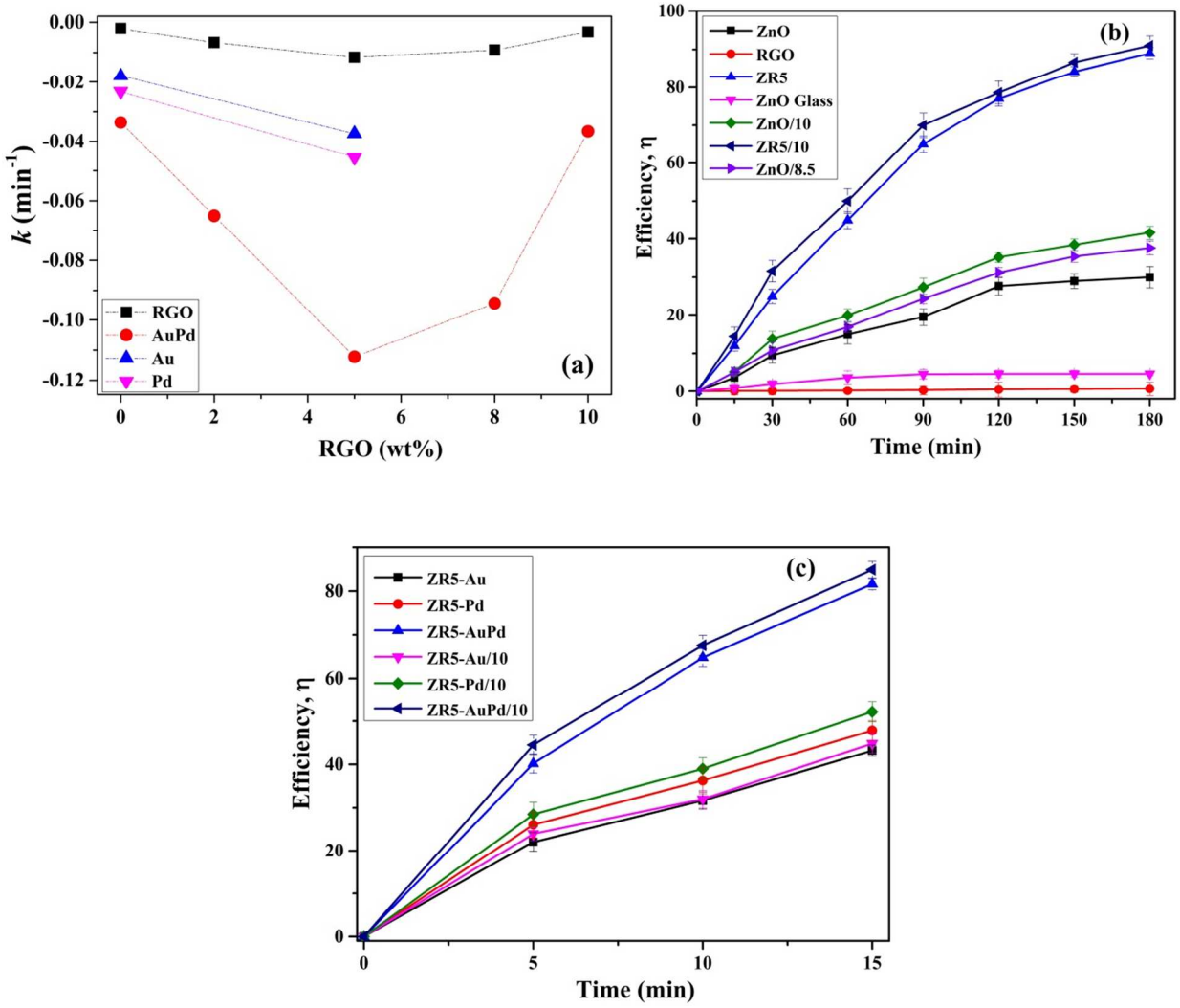


**Figure 7:** (a) Rate constant values of R6G photodegradation by using different photocatalysts. Photodegradation efficiency of (b) ZnO and 5 wt% RGO-ZnO, and (c) ZR5-Au, ZR5-Pd and ZR5-AuPd by varying pH of dye solution as a function of irradiation time.

**Scheme 1:** Schematic diagram showing possible mechanism involved in the generation of holes and hydroxyl radicals in ZR5 and ZR5-AuPd hybrid nanostructures for the photodegradation of R6G dye upon UV irradiation.

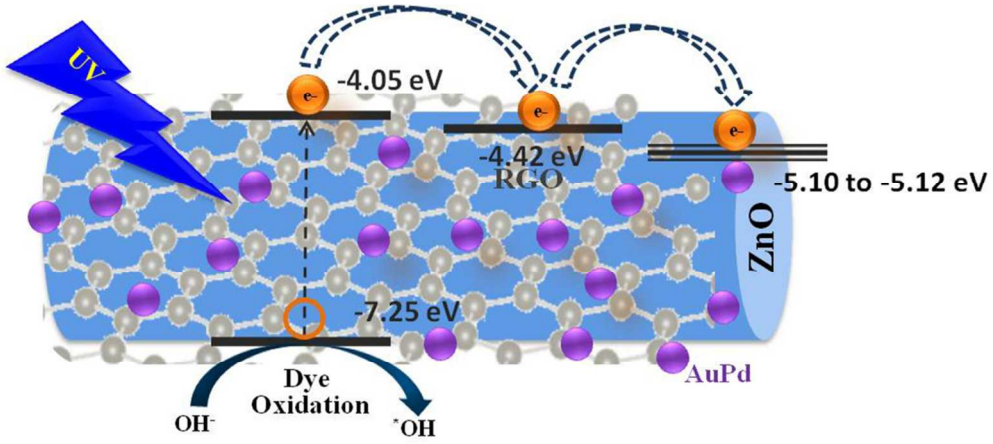


## References

1 C. A. Martínez-Huitle and S. Ferro, *Chem. Soc. Rev.*, 2006, **35**, 1324-1340.

2 R. W. Matthews, *J. Phys. Chem.*, 1987, **91,** 3328–3333.

3 P. X. Gao and Z. L. Wang, *J. Am. Chem. Soc.*, 2003, **125,** 11299–11305.

4 M. Ahmad and J. Zhu, *J. Mater. Chem.*, 2011, **21,** 599–614.

5 R. Viswanatha, S. Sapra, B. Satpati, P. V. Satyam, B. N. Dev and D. D. Sarma, *J. Mater. Chem.*, 2004, **14,** 661-668.

6 M. H. Huang, S. Mao, H. Feick, H. Q. Yan, Y. Y. Wu, H. Kind, E. Weber, R. Russo and P. Yang, *Science*, 2001, **292,** 1897-1899.

7 K. Park, Q. F. Zhang, B. B. Garcia, X. Y. Zhou, Y. H. Jeong and G. Z. Cao, *Adv. Mater.*, 2010, **22,** 2329−2332.

8 H. Zeng, W. Cai, P. Liu, X. Xu, H. Zhou, C. Klingshirn and H. Kalt, *ACS Nano*, 2008, **2(8),** 1661–1670.

9 H. Tong, S. Ouyang, Y. Bi, N. Umezawa, M. Oshikiri and J. Ye, *Adv. Mater.*, 2012, **24,** 229–251.

10 X. Bai, L. Wang, R. Zong, Y. Lv, Y. Sun and Y. Zhu, *Langmuir*, 2013, **29(9),** 3097–3105.

11 W. He, H. –K. Kim, W. G. Wamer, D. Melka, J. H. Callahan and J. –J. Yin, *J. Am. Chem. Soc.*, 2014, **136,** 750−757.

12 A. K. Geim and K. S. Novoselov, *Nat. Mater.*, 2007, **6,** 183-191.

13 Y. Zhang, J. W. Tan, H. L. Stormer and P. Kim, *Nature*, 2005, **438,** 201-204.

14 C. Lee, X. Wei, J. W. Kysar and J. Hone, *Science*, 2008, **321,** 385-388.

15 G. Liao, S. Chen, X. Quan, H. Yu and H. Zhao, *J. Mater. Chem.*, 2012, **22,** 2721-2726.

16 V. Stengl, D. Popelkova and P. Vlacil, *J. Phys. Chem. C*, 2011, **115,** 25209-25218.

17 V. Subramanian, E. E. Wolf and P. V. Kamat, *Langmuir*, 2003, **19,** 469−474.

18 Y. Yokomizoa, S. Krishnamurthy and P. V. Kamat, *Catal. Today*, 2013, **199,** 36–41.

19 P. Roy, A. P. Periasamy, C. –T. Liang and H. –T. Chang, *Environ. Sci. Technol.*, 2013, **47,** 6688−6695.

20 P. Fageria, S. Gangopadhyay and S. Pande, *RSC Adv.*, 2014, **4,** 24962–24972.

21 N. Morales-Flores, U. Pal and E. S. Mora, *Appl. Cat. A*, 2011, **394,** 269–275.

22 Y. Chen, D. Zeng, K. Zhang, A. Lu, L. Wang and D. –L. Peng, *Nanoscale*, 2014, **6,** 874–881

23 S. J. Chang, T. J. Hsueh, I. C. Chen, and B. R. Huang, *Nanotechnol.*, 2008, **19,** 175502.

24 X. H. Liu, J. Zhang, X. Z. Guo, S. H. Wu and S. R. Wang, *Nanoscale*, 2010, **2,** 1178–1184.

25 Z. H. Chen, Y. B. Tang, C. P. Liu, Y. H. Leung, G. D. Yuan, L. M. Chen, Y. Q. Wang, I. Bello, J. A. Zapien, W. J. Zhang, C. S. Lee and S. T. Lee, *J. Phys. Chem. C*, 2009, **113,** 13433-13437.

26 Y. Liu, M. Zhong, G. Shan, Y. Li, B. Huang and G. Yang, *J. Phys. Chem. B*, 2008, **112,** 6484–6489.

27 G. Shan, S. Wang, X. Fei, Y. Liu and G. Yang, *J. Phys. Chem. B*, 2009, **113,** 1468–1472.

28 S. Balachandran and M. Swaminathan, *Emer. Mater. Res.,* 2012, **1,** 157–163.

29 R. M. Ramli, C. F. Kait and A. A. Omar, *Adv. Mater. Res.*, 2013, **845,** 421-425.

30 Y. Shiraishi, H. Sakamoto, Y. Sugano, S. Ichikawa and T. Hirai, *ACS Nano*, 2013, **7(10),** 9287–9297.

31 A. Gallo, M. Marelli, R. Psaro, V. Gombac, T. Montini, P. Fornasiero, R. Pievod and V. D. Santo, *Green Chem.*, 2012, **14,** 330-333.

32 M. Tominaga, T. Shimazoe, M. Nagashima, H. Kusuda, A. Kubo, Y. Kuwahara and I. Taniguchi, *J. Electroanal. Chem.*, 2006, **590,** 37-46.

33 I. H. Yeo and D. C. Johnson, *J. Electroanal. Chem.*, 2001, **495,** 110-119.

34 J. Wang, D. F. Thomas and A. Chen, *Anal. Chem.*, 2008, **80,** 997-1004.

35 B. Panigrahy, M. Aslam and D. Bahadur, *J. Phys. Chem. C*, 2010, **114,** 11758-11763.

36 W. S. Hummers and R. E. Offeman, *J. Am. Chem. Soc.*, 1958, **80,** 1339-1339.

37 P. K. Sahoo, B. Panigrahy, D. Li and D. Bahadur, *J. Appl. Phys.*, 2013, **113,** 17B525-(1-3).

38 K. Gotoh, T. Kinumoto, E. Fujii, A. Yamamoto, H. Hashimoto, T. Ohkubo, A. Itadani, Y. Kuroda and H. Ishida, *Carbon*, 2011, **49,** 1118-25.

39 D. Sun, G. Zhang, X. Jiang, J. Huang, X. Jing, Y. Zheng, J. He and Q. Li, *J. Mater. Chem. A*, 2014, **2,** 1767–1773.

40 P. K. Sahoo, B. Panigrahy and D. Bahadur, *RSC Adv.*, 2014, **4,** 48563- 48571.

41 W. Xitao, L. Rong and W. Kang, *J. Mater. Chem. A*, 2014, **2,** 8304-8313.

42 D. R. Dreyer, S. Park, C. W. Bielawski and R. S. Ruoff, *Chem. Soc. Rev.*, 2010, **39,** 228−240.

43 N. J. Bell, H. N. Yun, A. J. Du, H. Coster, S. C. Smith and R. Amal, *J. Phys. Chem. C*, 2011, **115,** 6004−6009.

44 S. S. Lo and D. Huang, *Langmuir*, 2010, **26,** 6762−6766.

45 H. M. Song, B. A. Moosa and N. M. Khasha, *J. Mater. Chem.*, 2012, **22,** 15953–15959.

46 Y. Zhang, N. Zhang, Z. –R. Tang and Y. –J. Xu, *J. Phys. Chem. C*, 2014, **118,** 5299−5308.

47 J. Wu, X. Shen, L. Jiang, K. Wang and K. Chen, *Appl. Surf. Sci.*, 2010, **256,** 2826–2830.

48 X. Wang, L. J. Zhi, N. Tsao, J. L. Tomovic and K. Mullen, *Angew. Chem. Int. Ed.*, 2008, **47,** 2990–2992.

49 J. J. Schneider, R.C. Hoffmann, J. Engstler, O. Soffke, A. Issanin and A. A. Klyszcz, *Adv. Mater.*, 2008, **20,** 3383–3387.

50 R. Viswanatha, S. Sapra, B. Satpati, P. V. Satyam, B. N. Dev and D. D. Sarma, *J. Mater. Chem.*, 2004, **14,** 661-668.

51 B. Panigrahy, M. Aslam and D. Bahadur, *Appl. Phys. Lett.*, 2011, **98,** 183109-(1-3).

52 B. Panigrahy, M. Aslam, D. S. Misra, M. Ghosh and D. Bahadur, *Adv. Funct. Mater.*, 2010, **20,** 1161-1165.

53 D. Shao, H. Sun, J. Gao, G. Xin, M. A. Aguilar, T. Yao, N. Koratkar, J. Lian and S. Sawyer, *Nanoscale*, 2014, **6,** 13630–13636.

54 M. A. Behnajady, N. Modirshahla and R. Hamzavi, *J. Hazard. Mater.*, 2006, **B133,** 226–232.

55 D. Bahnemann, *Solar Energy,* 2004, **77,** 445-459.

56 M. D. L. Ruiz Peralta, U. Pal and R. S. Zeferino, *Appl. Mater. Interfaces*, 2012, 4, 4807−4816.

57 Y. Feng, N. Feng, Y. Wei and G. Zhang, *RSC Adv.*, 2014, **4,** 7933–7943.

58 S. A. Ansari, M. M. Khan, M. O. Ansari, J. Lee and M. H. Cho, *J. Phys. Chem. C*, 2013, **117,** 27023-27030.

59 R. Saravanan, N. Karthikeyan, V. K. Gupta, E. Thirumal, P. Thangadurai, V. Narayanan and A. Stephen, *Mater. Sci. Eng. C*, 2013, **33,** 2235-2244.

60 R. Su, R. Tiruvalam, A. J. Logsdail, Q. He, C. A. Downing, M. T. Jensen, N. Dimitratos, L. Kesavan, P. P. Wells, R. Bechstein, H. H. Jensen, S. Wendt, C. Richard, A. Catlow, C. J. Kiely, G. J. Hutchings and F. Besenbacher, *ACS Nano*, 2014, **8(4),** 3490–3497.

61 D. O. Scanlon, C. W. Dunnill, J. Buckeridge, S. A. Shevlin, A. J. Logsdail, S. M. Woodley, C. R. A. Catlow, M. J. Powell, R. G. Palgrave, I. P. Parkin, G. W. Watson, T. W. Keal, P. Sherwood, A. Walsh and A. A. Sokol, *Nat. Mater.*, 2013, **12,** 798–801.

62 S. K. Kansal, M. Singh and D. Sud, *J. Hazard. Mater.*, 2007, **141,** 581–590.

63 N. Udawatte, M. Lee, J. Kim, D. Lee, *ACS Appl. Mater. Interfaces*, 2011, **3,** 4531–4538.